

Raman spectroscopic carbonaceous material thermometry of low-grade metamorphic rocks: Calibration and application to tectonic exhumation in Crete, Greece

Jeffrey M. Rahl^{a,c,*}, Kristin M. Anderson^a, Mark T. Brandon^a, Charalambos Fassoulas^b

^a Department of Geology and Geophysics, Yale University, P.O. Box 208109, New Haven, CT 06520-8109, USA

^b Natural History Museum of Crete, University of Crete, Heraklion 71409, Greece

^c Department of Geological Sciences, University of Michigan, 2534 C.C. Little Building, 1100 N. University Ave., Ann Arbor, MI 48109-1005, USA

Received 6 December 2004; received in revised form 5 August 2005; accepted 21 September 2005

Available online 2 November 2005

Editor: K. Farley

Abstract

We present new Raman spectra data of carbonaceous material (CM) to extend the range of the Raman spectra of CM thermometer (RSCM) to temperatures as low as 100 °C. Previous work has demonstrated that Raman spectroscopy is an excellent tool to describe the degree of graphitization of CM, a process that is independent of pressure but strongly dependent on metamorphic temperature. A linear relationship between temperature and the Raman parameter R2 (derived from the area of the defect band relative to the ordered graphite band) forms the basis of a previous thermometer. Because R2 shows little variability in low-temperature samples, 330 °C serves as a lower limit on the existing thermometer. Herein, we present Raman spectra from a suite of low-temperature (100 to 300 °C) samples from the Olympics Mountains and describe other aspects of the Raman spectra of CM that vary over this range. In particular, the Raman parameter R1 (the ratio of heights of the disordered peak to ordered peak) varies regularly between 100 and 350 °C. These data, together with published results from higher-temperature rocks, are used to calibrate a modified RSCM thermometer, applicable from 100 to 700 °C. Application to low-grade metasediments in the Otago region in the South Island of New Zealand gives temperatures consistent with previous estimates, demonstrating the reliability of the modified RSCM thermometer.

We apply the modified RSCM thermometer to 53 samples from Crete to evaluate the role of the Cretan detachment fault in exhuming Miocene high pressure/low-temperature metamorphic rocks exposed there. The metamorphic rocks below the detachment (the Plattenkalk and Phyllite–Quartzite units) give metamorphic temperatures that range from 250 to 400 °C, consistent with previous petrologic estimates. We also demonstrate that the Tripolitza unit, which lies directly above the detachment, gives an average metamorphic temperature of about 260 °C. The modest break in metamorphic temperature in central Crete indicates that the Cretan detachment accounts for only 5 to 7 km of exhumation of the underlying HP–LT metamorphic rocks, which were initially accreted at ~35 km. We argue that the bulk of the exhumation (~28 km out of 35 km total) occurred by pervasive brittle stretching and erosion of structural units above the detachment.

© 2005 Elsevier B.V. All rights reserved.

Keywords: Crete; graphitization; Raman spectroscopy; geothermometry

* Corresponding author. Department of Geological Sciences, University of Michigan, 2534 C.C. Little Building, 1100 N. University Ave., Ann Arbor, MI 48109-1005, USA.

E-mail address: jrahl@umich.edu (J.M. Rahl).

1. Introduction

The progressive graphitization of carbonaceous material (CM) with increasing temperature forms the basis of a metamorphic thermometer for metasedimentary rocks [1–3]. Sedimentary rocks generally contain trace amounts of initially poorly ordered CM, which transforms into well-ordered graphite with increasing metamorphic grade [4–7]. Laser Raman spectroscopy is a tool to directly measure the degree of ordering of CM [6,8–10]. Raman analysis is quick and applicable to both rock chips and standard petrographic thin sections.

Beysac et al. [1] were the first to formulate an empirical metamorphic thermometer using Raman spectroscopy of CM (RSCM). They demonstrated that CM crystallinity is strongly correlated with peak metamorphic temperature but not with metamorphic pressure. The thermometer is based on an observed linear relation between metamorphic temperature and the R2 parameter, which is the ratio of the peak areas for the disordered and ordered bands as measured in the CM Raman spectra. Their RSCM thermometer works best for samples with metamorphic temperatures between 330 and 650 °C, a range over which R2 progressively decreases from about 0.7 to less than 0.05. However, R2 varies little outside of this temperature range and measurements at the limits of this R2 range cannot be confidently assigned a temperature. Yui et al. [7] showed that other aspects of the Raman spectra do change systematically for metamorphic temperatures less than 330 °C. This observation suggests that the RSCM thermometer could be extended to work over a larger temperature range.

Beysac et al. [1] showed that the degree of graphitization is unaffected by retrograde metamorphic events. Therefore, the metamorphic transformation from organic carbon to graphite is largely an irreversible process and estimated temperatures should approximate peak metamorphic conditions. In detail, the situation is likely more complicated. Graphitization is a kinetically controlled process, and it takes millions of years to heat a rock up to metamorphic conditions and a similar amount of time to cool down. Our understanding of other similar kinetic processes suggests that reaction rate probably increases in a highly nonlinear fashion with increasing temperature (e.g., [11,12]). Thus the degree of transformation is probably strongly weighted to the duration of time at peak temperature, a conclusion supported by experiments [13]. The RSCM thermometer is empirically calibrated using samples with known “peak temperatures” as estimated using metamorphic petrology. As a result, the RSCM temperature estimates are probably best called “metamorphic temperatures” in that they are rep-

resentative of the peak temperature estimates that we might otherwise obtain from metamorphic thermometry.

In this paper, we introduce and calibrate a modified version of the RSCM thermometer using Raman spectra from CM in samples from the Olympic Mountains in Washington State. Apatite and zircon fission-track samples from the Olympic subduction wedge show various degrees of thermal resetting and therefore constrain metamorphic temperatures achieved during Miocene accretion [14]. The modified RSCM thermometer provides reliable temperature estimates between 100 and 700 °C. We demonstrate the reliability of the thermometer through application to a metamorphic sequence in New Zealand. We then use the modified thermometer to study tectonic exhumation of the Hellenic subduction wedge exposed on the Island of Crete, Greece [15–19].

2. Data acquisition and treatment

Laser Raman measurements of CM were made using standard petrographic thin sections for samples from Crete and New Zealand or using polished rock sections for the Olympics samples. Raman measurements of graphitic CM varies with mineral orientation [20], but the effects of this anisotropy are reduced by measuring the CM particles along their edges in oriented thin sections or rock chips [1]. Sections were generally cut normal to the macroscopic foliation (if present) and parallel to any stretching lineation. For samples without a clear deformation fabric, sections were cut normal to bedding.

Raman microspectroscopy was measured using a LABRAM spectrometer from the company Jobin Yvon with a Nd-YAG 532 nm laser source and a Peltier-cooled CCD detector. The laser was focused on the sample with a 500 nm confocal hole using the 100× objective under both reflected and transmitted light. The spot on the sample was ~1.5 μm in diameter and had a power of ~1 mW at the sample surface. Jobin Yvon’s LabSpec program was used for data acquisition and estimation of Raman peaks. To avoid bias caused by mechanical polishing, the laser was focused on CM beneath adjacent translucent grains, such as quartz [13,21]. A minimum of 10 independent spots were analyzed on each sample and data were collected from 5 to 60 s per spot depending upon the Raman intensity. The sample was measured over a spectral window of 1000 to 1800 cm⁻¹; replicate analyses over a larger spectral window (700 to 2000 cm⁻¹) indicate that the smaller window was of sufficient size to estimate the baseline for the spectra. The spectra were decomposed into bands (discussed below) and means and standard errors were calculated for the relevant parameters for each sample (Table 1).

CM is best characterized by first-order Raman peaks or bands, which occur with wavenumber offsets between 1000 and 1800 cm^{-1} [1,8,13]. CM has up to four bands in this range, including the G band (centered at about 1580 cm^{-1}) and three defect bands, located at about 1350 cm^{-1} for D1, 1620 cm^{-1} for D2, and 1510 cm^{-1} for D3 (Fig. 1). Peak shape is well defined by a Voigt function. The LabSpec program was used to estimate essential parameters for each of the four peaks: mean, height, full width at half maximum (FWHM), and area [13]. The degree of order in the CM is represented by two ratios [1,13],

$$R2 = \left(\frac{D1}{G + D1 + D2} \right)_A \quad (1)$$

and

$$R1 = \left(\frac{D1}{G} \right)_H \quad (2)$$

The subscripts A and H indicate that the ratio is based on peak areas and peak heights, respectively. Raman spectroscopy provides only a relative measurement in that intensity can vary with time and with sample characteristics. The ratios R1 and R2 remove the effect of this variation. The R1 and R2 values estimated for each sample are determined by converting the individual spot measurements into R1 and R2 values and then averaging those values. Raman data and temperature estimates for the samples discussed here are fully reported in Appendix A.

3. Calibration samples from Olympic mountains

Eleven samples from the Olympic Mountains in Washington State are used to calibrate the RSCM thermometer for very-low-grade metamorphic conditions. The Olympics mark the forearc high of the Cascadia

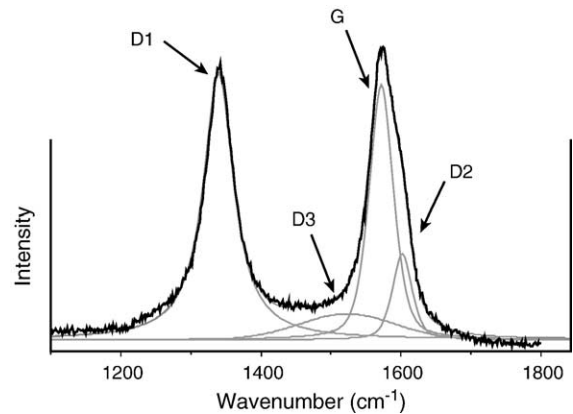


Fig. 1. An example Raman spectrum of CM from sample 000626-3 from western Crete, illustrating how the results are deconvoluted into four distinct peaks.

subduction zone and expose a sequence of siliciclastic sediments that were deformed and metamorphosed over the last 20 m.y. [14,22,23]. Focused erosion on the center of the uplift has caused a “bull’s-eye” map pattern with metamorphic grade increasing towards the center of the range. The thermal history of the region is well-known through an extensive suite of fission-track (FT) and (U-Th)/He ages [14,23–25].

Fig. 2(A–C) shows the pattern of resetting for these thermochronometers. All (U-Th)/He apatite ages in the region are reset, indicating that peak temperatures are $> \sim 60$ °C throughout most of the area [23]. In contrast, fission-track (FT) ages of apatite and zircon show various degrees of resetting, which can be characterized by comparing the FT grain age (FTGA) distribution with the depositional age of the sample [14]. The grain ages themselves have low precision, so FTGA distributions were decomposed into concordant grain age components, called peaks. Zircon and apatite both have heterogeneous properties for annealing of fission tracks, with

Table 1

Samples from Olympic Mountains used for low temperature calibration of the RSCM thermometer

Laboratory number	Apatite FT	Zircon FT	Temperature (°C)	±	Latitude (°N)	Longitude (°E)
9	Reset	Partially reset	250	50	47.779	236.422
14	Mixed reset	Partially reset	250	50	47.795	236.302
17	Reset	Partially reset	250	50	47.789	236.365
22	Partially reset	Detrital	115	25	47.556	236.333
48	Reset	Partially reset	250	50	47.794	236.639
49	Mixed reset	Detrital	170	30	47.791	236.709
106	Reset	Detrital	170	30	48.079	235.700
107	Reset	Detrital	170	30	47.980	235.609
33	Partially reset	Detrital	115	25	47.877	236.855
40	Mixed reset	Detrital	170	30	47.813	236.019
42b	Partially reset	Detrital	115	25	47.640	236.615

See Appendix A for Raman data of these samples.

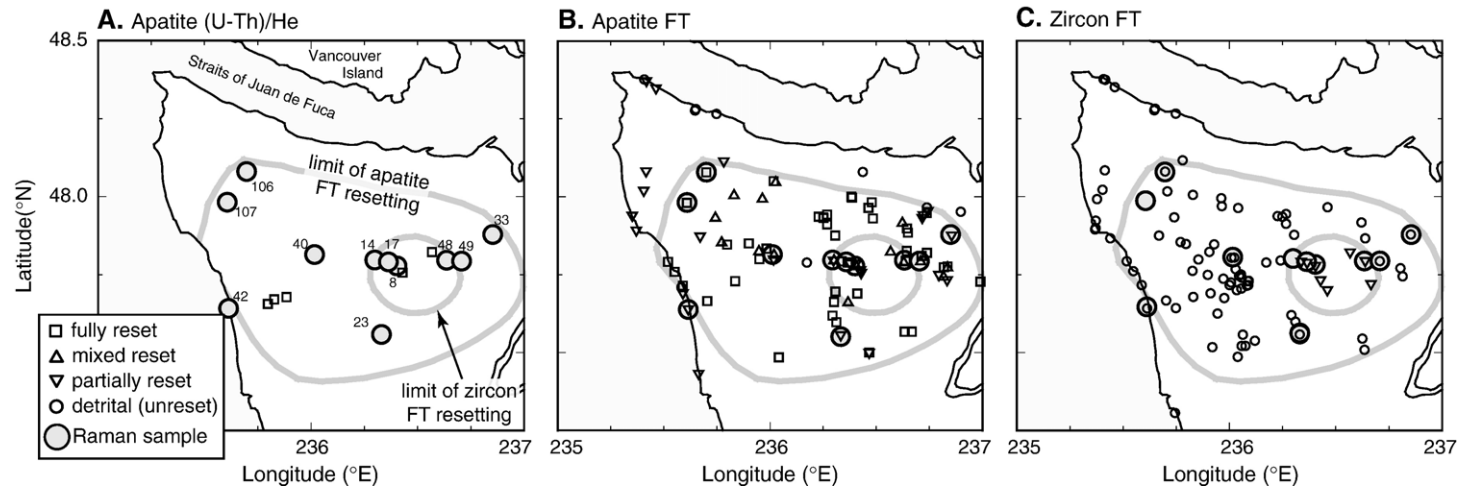


Fig. 2. Maps of the Olympic Mountains area, showing locations of Raman samples (large circles) and variably reset FT and (U-Th)/He ages. The symbols for the FT and He ages indicate the degree of resetting (D, PR, MR, and R, as discussed in text). The outer gray line encloses all reset apatite FT ages (MR- and R-type distributions), indicating metamorphic temperatures >140 °C. The inner gray line encloses all reset zircon FT ages (PR-type distributions), indicating metamorphic temperatures >200 °C. (A) (U-Th)/He apatite ages (small squares) [23], all of which are fully reset, indicating metamorphic temperatures >60 °C. (B) Apatite FT ages ([14, 23] and unpublished data of Mary Roden-Tice and Mark Brandon). (C) Zircon FT ages ([24,25] and unpublished data of Richard Stewart and Mark Brandon).

radiation damage and composition providing the main controls [26–28]. This factor is important for dating sedimentary rocks since the detrital apatites and zircons are derived from many sources. As a result, sandstones commonly yield FTGA distributions with multiple peaks, even when largely reset. In the Olympic Mountains, both reset and unreset apatite FTGA distributions typically have no more than two peaks. Unreset Zircon FTGA distributions can have up to four peaks and commonly preserve two peaks after resetting.

Brandon et al. [14] identified four stages of resetting for apatite FT ages in the Olympic Mountains (Fig. 2B). 1) *Detrital (D) samples* are unreset, given that all of the FT peak ages are older than the depositional age of the sandstone. 2) *Partially reset (PR) samples* have multiple FT peaks with one peak younger than deposition. 3) *Mixed reset (MR) samples* have multiple FT peaks with all peaks younger than deposition. 4) *Reset single-peak (R) samples* have a single FT peak with an age younger than deposition. We interpret these changes to a record greater resetting with increasing maximum temperature.

We used the AFTSolve program [29] to estimate the maximum temperature as a function of resetting of the apatite FT ages. Chlorine substitution represents the primary factor influencing the track annealing properties of apatite. In our model, detrital apatites are represented by a compositional range of 0 to 0.4 cation fraction of chlorine substitution per apatite formula unit, which is equivalent to the 95% range for detrital apatites reported in [27]. We use stepwise heating of 5 to 10 m.y., which is representative of the duration of heating for the Olympics [23]. For these samples, a reduction in age of about 50% is required to reduce detrital ages to less than the age of deposition, which we take to represent a significant amount of resetting.

AFTSolve indicates that the least retentive apatites show about 50% reduction in age when subjected to temperatures of ~ 90 °C for 5 to 10 m.y. In contrast, the most retentive apatites require temperatures of ~ 140 °C to produce the same amount of resetting. Thus, we infer the maximum temperatures for apatite samples with D-type FTGA distributions to be < 90 °C, for those with PR-type distributions to be from 90 to 140 °C, and for those with MR- and R-type distributions to be > 140 °C.

In the Olympic Mountains, zircon FT ages only show D-type and PR-type distributions (Fig. 2C). The PR-type samples are located in the central and most deeply eroded part of the Olympics (outlined by the inner gray line in Fig. 2). Brandon and Vance [24] and Brandon et al. [14] estimate that the transition for zircon FT ages from D- to PR-type distributions occurs at about 200 °C, given the time–temperature path associ-

ated with subduction and exhumation in the Olympics [23] and the annealing behavior of fission-tracks in radiation-damaged zircons [14,24,30]. The older peaks in the PR-type samples are attributed to young detrital zircons in the samples, which had low radiation damage at the time of thermal resetting and thus a greater ability to retain fission tracks. Temperatures $> \sim 300$ °C are needed to produce a 50% reduction in age for zero-damage zircons subjected to a 5 to 10 m.y. heating event [30]. Thus, we infer a maximum temperature of < 200 °C for zircon samples with D-type distributions and a temperature between 200 °C and 300 °C for samples with PR-type distributions.

These constraints are used to assign maximum temperatures for the samples used to calibrate the RSCM thermometer (Table 1). The midpoint is considered the best estimate and the range is taken as the uncertainty.

4. Revised calibration of the RSCM thermometer

Beysac et al. [1] based their RSCM thermometer on the observed linear relationship between metamorphic temperature and R2. This relationship breaks down, however, below 330 °C (Fig. 3A). In fact, an R2 value of 0.7 to 0.8 can only be taken as evidence that the metamorphic temperature was < 330 °C. Our Olympic samples have metamorphic temperatures that range from 115 to 250 °C (Table 1), and R2 shows no variation, remaining steady at ~ 0.75 .

Yui et al. [7] measured RSCM for a metamorphic sequence in Taiwan that ranges from zeolite to greenschist facies. They fit their spectra for the G, D1, and D2 bands, but not the D3 band. As a result, their estimates of D2 and G are biased upward and cannot be directly compared with our measurements or those of Beysac et al. [1]. Nonetheless, their study shows a clear evolution even at these low metamorphic temperatures. As metamorphic grade increases, the width of their D1 decreases from ~ 200 cm^{-1} to ~ 100 cm^{-1} , and their $(\text{D1/G})_A$ decreases from ~ 2.0 to less than 1.0. Their ratio $(\text{D1/G})_H$ (similar to R1 used here) increases from ~ 0.5 to ~ 2.1 in the transition from zeolite to lower greenschist facies, and then decreases at higher grades. The combination of our Olympic samples and those from Beysac et al. [1] provides a quantitative calibration of this transition, with R1 (Figs. 3B and 4) increasing from ~ 0.5 at 115 °C to ~ 2.1 at 250 °C and then decreasing at higher metamorphic temperatures.

We report here a modified RSCM thermometer, based on both R1 and R2 and calibrated using the combined data from Beysac et al. (2002) and the Olympic Mountains. These data sets have similar mea-

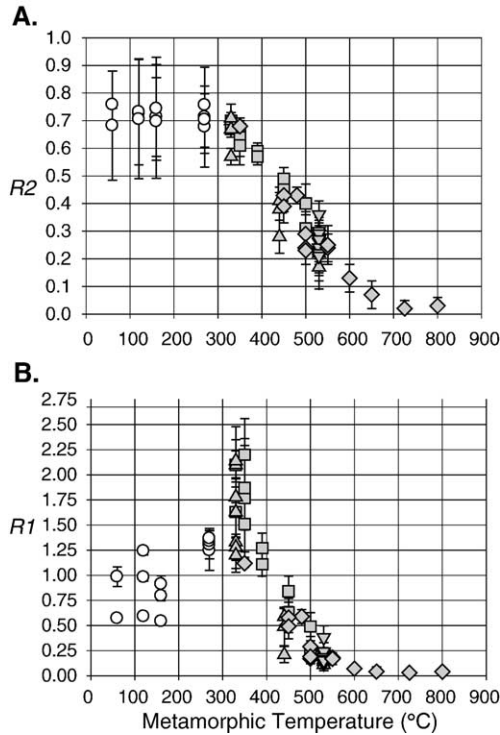


Fig. 3. R2 and R1 versus independently estimated temperature. White circles denote samples from the Olympics (this study); gray symbols are data from [1]. The different shapes correspond to different settings: squares from western Alps; triangles from Japan, overturned triangles from Tinos, Greece; and diamonds are individual samples from a variety of settings. Beysac et al. [1] demonstrate a linear correlation in R2 over the range 330 to 600 °C, but there is little variation in R2 for temperatures over low temperatures. In contrast, R1 increases over the low-temperature range. Error bars show the standard error for each estimate.

surement errors, with standard errors of $SE(T) \sim 16$ °C, $SE(R1) \sim 0.059$, and $SE(R2) \sim 0.0160$. Note that we have taken $\pm 2 SE(T)$ as equal to the uncertainty range for T , as cited, for example, in Table 1. Estimates of $SE(R1)$ and $SE(R2)$ were determined from the standard deviation for the replicated spot measurements divided by the square root of the number of replicates. We measured 10 spots per sample, whereas Beysac et al. [1] measured between 10 and 15. Average SEs were calculated using the quadratic mean.

We used unweighted regression to search for a generic polynomial function that best fit the data, with T as the dependent variable. In conventional regression analysis, the best fit is found by minimizing the misfit relative to the dependent variable. This assumes that all error resides in the dependent variable, which is T in the case here. Rantitsch et al. [3] argue that the RSCM thermometer should instead be calibrated using a more general approach where the fit is weighted using the SEs for all of the variables in the calibration data and not just

the T . This approach is preferred if we want to make unbiased estimates of the unknown parameters in the fit equation. However, our goal is to design a calibration equation that will provide reliable predictions of T from measurements of R1 and R2. The parameter bias that sometimes arises from the conventional regression solution has little effect on the prediction performance of a calibration equation [31]. When using conventional regression for calibration, the variable to be predicted is assigned as the dependent variable, and the regression analysis is used to find the parameters for the calibration equation. The calibration equation determined by this regression will provide unbiased predictions of T if the R1 and R2 measurements used to predict T lie within the range of the R1 and R2 values used for the calibration and were acquired in the same way (i.e., the standard errors for R1 and R2 are similar to those for the calibration). The issues discussed here are referred to as the “error-in-variables” problem and the “calibration” problem (for a good introduction to these issues, see [31–37]).

The calibration data set used here is best fit by a bivariate polynomial function

$$T(^{\circ}\text{C}) = 737.3 + 320.9 R1 - 1067 R2 - 80.638 R1^2, \quad (3)$$

with the fit parameter $R^2=0.94$. The relationship of this function to the data is shown in Fig. 5. The F test (p.

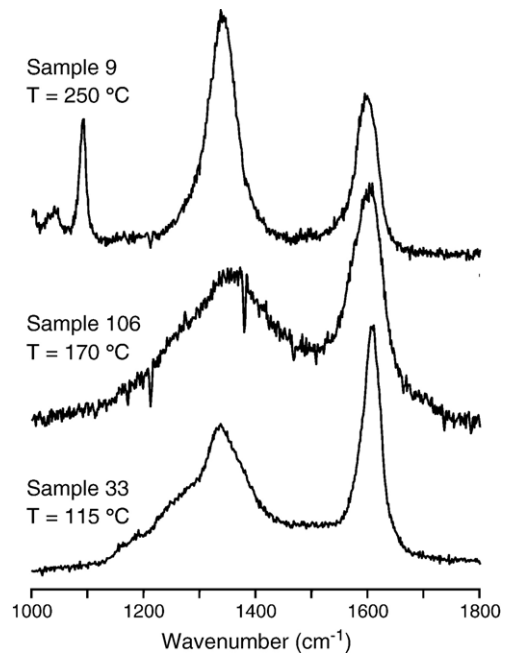


Fig. 4. Raman spectra for CM from representative low-grade samples, illustrating a progressive increase in R1 (the height ratio of the disordered to ordered peak) with temperature. At higher temperatures (not shown), the D1 peak decreases and ultimately disappears [1].

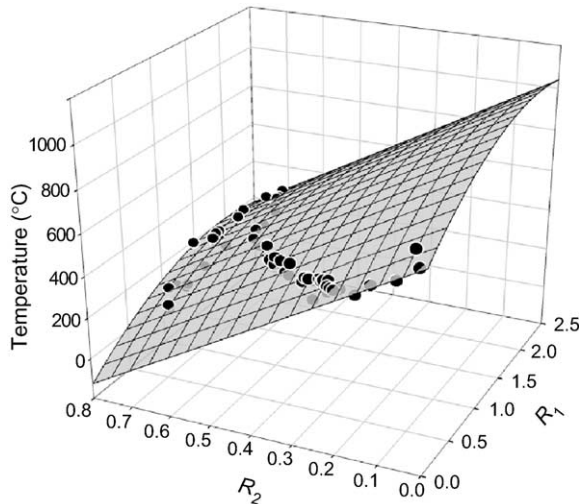


Fig. 5. Three-dimensional plot showing the calibration data and best-fit surface.

200 in Bevington [38]) indicates that the functional form of Eq. (3) fits the data better than other close alternatives, such as a planar equation (with no $R1^2$ term) or a full quadratic polynomial (with the addition of an $R2^2$ term).

The residuals provide another indicator of the quality of the fit (symbols in Fig. 6). These appear to be randomly distributed relative to T and have a standard deviation of $36.7\text{ }^\circ\text{C}$. Propagation of the standard errors for $R1$, $R2$, and T through Eq. (3) indicates that these measurement errors would produce a standard deviation in the residuals of $27.0\text{ }^\circ\text{C}$. The difference between these two standard deviations ($36.7\text{ }^\circ\text{C}$ vs. $27.0\text{ }^\circ\text{C}$) indicates that, in addition to measurement errors, there are other significant sources of error with a standard deviation of $\sim 25\text{ }^\circ\text{C}$. These other errors are probably due to natural factors or to “equation error” [33,36].

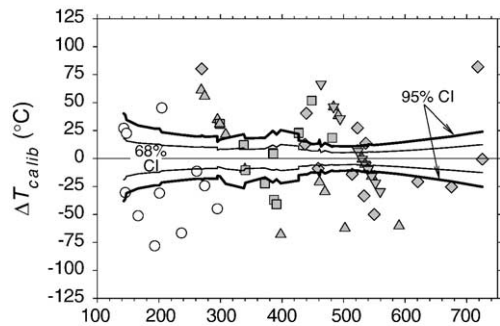
A bootstrap analysis [39] was used to estimate confidence intervals for the calibration of Eq. (3) and the prediction of T (Fig. 6). Sampling was done using the “non-parametric method” and confidence intervals were estimated using the “basic method” [40]. The analysis involved the following steps:

- 1) The calibration data were resampled at random (with replacement) to generate a new replicate data set of 65 observations.
- 2) This “new” data set was used to calculate a new fit for the calibration Eq. (3).
- 3) Each of the 65 $R1$, $R2$ pairs from the calibration data set was used to generate new temperature estimates. We recorded these 65 values as ΔT_{calib} , equal to the difference between the estimated tem-

peratures and those predicted from the original calibration, as given by Eq. (3). The ΔT_{calib} values represent the *calibration error*, which is the uncertainty in estimates of T due solely to the errors in calibrating Eq. (3).

- 4) We then generated a new replicate set of $R1$, $R2$ measurements. It is important that our analysis is restricted to the range of $R1$, $R2$ values used in the calibration, as the predictions are only valid over that range. Thus, we used as “true values” the $R1$, $R2$ pairs from the calibration data set. The replicated “observed values” were generated by adding normal deviates with zero means and standard deviations equal to the $SE(R1)$ and $SE(R2)$, as reported above. These values were then used to predict T using the current calibration Eq. (3) from step #2. We recorded

A. Calibration Error



B. Prediction Error

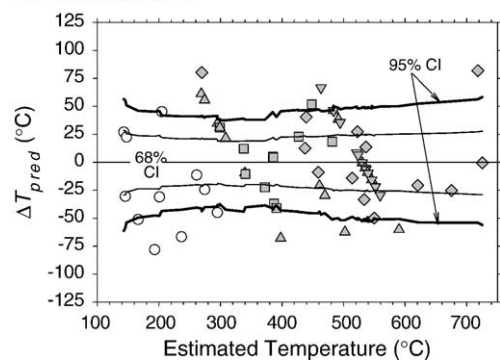


Fig. 6. Estimated uncertainties for the modified RSMC thermometer. The light and heavy lines show confidence intervals (CI) at probabilities of 68% and 95%, respectively. (A) The *calibration errors* plot shows the uncertainties related to estimation of the calibration Eq. (3). (B) The *prediction errors* plot shows the full uncertainties for the prediction of an unknown T from measurements of $R1$ and $R2$. These uncertainties include the calibration errors from (A), plus the errors for the $R1$ and $R2$ measurements used to estimate the unknown T . Note that the prediction uncertainties assume that measurement errors associated with the $R1$ and $R2$ values for an unknown are similar to those used for the calibration. ΔT_{calib} and ΔT_{pred} are defined as the difference between the observed and estimated temperatures for the *calibration errors* analysis and the *prediction errors* analysis, respectively.

the 65 ΔT_{pred} values, equal to the difference between the current temperature predictions and those predicted from the original calibration Eq. (3). These values represent the *prediction error*, which includes all of the errors associated with prediction of T from R1 and R2, including the calibration error for Eq. (3) and the measurement errors for the R1 and R2 values used to predict T .

- 5) Steps 1 to 4 were repeated 10,000 times. When finished, each R1, R2 pair from the calibration data set had 10,000 replicates for ΔT_{calb} and 10,000 replicates for ΔT_{pred} . These distributions were used to represent the calibration and prediction errors expected for each R1, R2 pair. We show these results in Fig. 6, where the R1, R2 pairs are represented by the T predicted from (3). The lines in Fig. 6A and B show ΔT_{calb} and ΔT_{pred} values at 2.5%, 16%, 84%, and 97.5% cumulative probability for the distributions generated for each R1, R2 pairs. These probabilities were selected to represent the conventional 68% and 95% confidence intervals.

The bootstrap analysis indicates that Eq. (3) predicts temperatures to ± 50 °C at the 95% confidence level (Fig. 6B). We emphasize that this prediction is entirely empirical, with Eq. (3) merely providing a mapping from measured values of R1 and R2 to predicted values of T . The broader success of the revised RSCM thermometer depends on the critical assumption that the calibration data are representative of the behavior of RSCM in all metamorphic rocks. Further calibration using other metamorphic settings will help test this assumption.

5. Applications

5.1. Otago subduction complex, South Island, New Zealand

We test the modified RSCM thermometer with samples from a metamorphic sequence of sandstones and mudstones exposed in the Otago high, a broad antiform about 150 km across and which trends roughly east–west across the South Island of New Zealand [41]. The Otago region marks the forearc high of a Mesozoic subduction wedge that formed along the eastern margin of Gondwana [42–44]. The sediments were deeply accreted, metamorphosed, and then exhumed with the deepest rocks exposed in the core of the uplift. The distribution of metamorphic assemblages is well known [45], but thermobarometric measurements are sparse because diagnostic metamorphic assemblages are gen-

erally not present. Maximum P – T conditions are estimated to be 0.8–1.0 GPa and 350–450 °C for rocks exposed in the core [45]. Metamorphic grade decreases continuously towards the flanks of the uplift, where the lowest grade rocks are prehnite–pumpellyite facies [45]. Apatite FT ages [46] are everywhere reset, indicating that all of the currently exposed rocks experienced metamorphic temperatures $> \sim 125$ °C. Further use of FT data to estimate metamorphic temperatures is hampered because grain ages were not reported for the FT apatite data and published FT zircon ages are sparse.

We have applied the RSCM technique to 14 samples from Otago that come from prehnite–pumpellyite to greenschist facies (Fig. 7). Previous X-ray diffraction work has shown that the degree of graphitization varies smoothly across the region and correlates with peak metamorphic conditions [47]. Our data give metamorphic temperatures that are consistent with the observed metamorphic grade. In the lowest grade rocks along the flanks of the uplift, metamorphic temperatures are generally between 100 and 200 °C. Metamorphic temperature increases towards the core, reaching values of 475 °C, which is consistent with estimates of peak temperatures of 350–450 °C [45]. The similarity of these estimates supports the use of the modified RSCM method for predicting metamorphic temperatures as low as 120 °C.

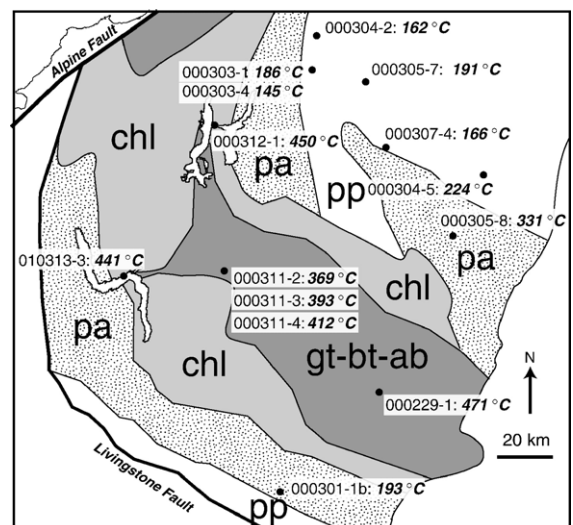


Fig. 7. Map of the Otago region of the South Island, New Zealand. Metamorphic facies after Mortimer [41,45]; pp: prehnite–pumpellyite; pa: pumpellyite–actinolite; chl, greenschist facies chlorite zone; gt–bi–ab; greenschist facies garnet–biotite–albite zone. Black points show sample locations for the RSCM metamorphic temperatures reported here. See Appendix A for the detailed Raman data table.

5.2. Crete, Greece

Crete marks the forearc high of the modern Hellenic subduction zone in the eastern Mediterranean. Continuous northward subduction of the African plate since at least 40 Ma has driven accretion and growth of a large south-facing subduction wedge, which includes both Crete and the Mediterranean Ridge [48,49]. Crete is made up of a structural sequence of sedimentary units that were imbricated and accreted in the Oligocene (e.g., [50,51]). Several of the units were deeply subducted and underplated at the base of the wedge and record deformation and metamorphism that culminated at 20 to 25 Ma [15–18,48].

The structural sequence is composed of a well-ordered set of coherent thrust sheets or nappes. The sequence has been divided into two parts based on metamorphic history and structural position (Fig. 8) [15,17–19]. The lower part contains two main structural units (from lowest to highest): the Plattenkalk (PK) nappe and the Phyllite–Quartzite (PQ) nappe, both of which were metamorphosed under high pressure–low temperature (HP–LT) conditions [15,16]. These HP–LT metamorphic units are separated from higher structural units by the low-angle Cretan detachment fault (Fig. 9) [17,18,52]. Above the detachment are three main structural nappes (from lowest to highest): the Tripolitza, the Pindos, and the Uppermost units. Generally these units

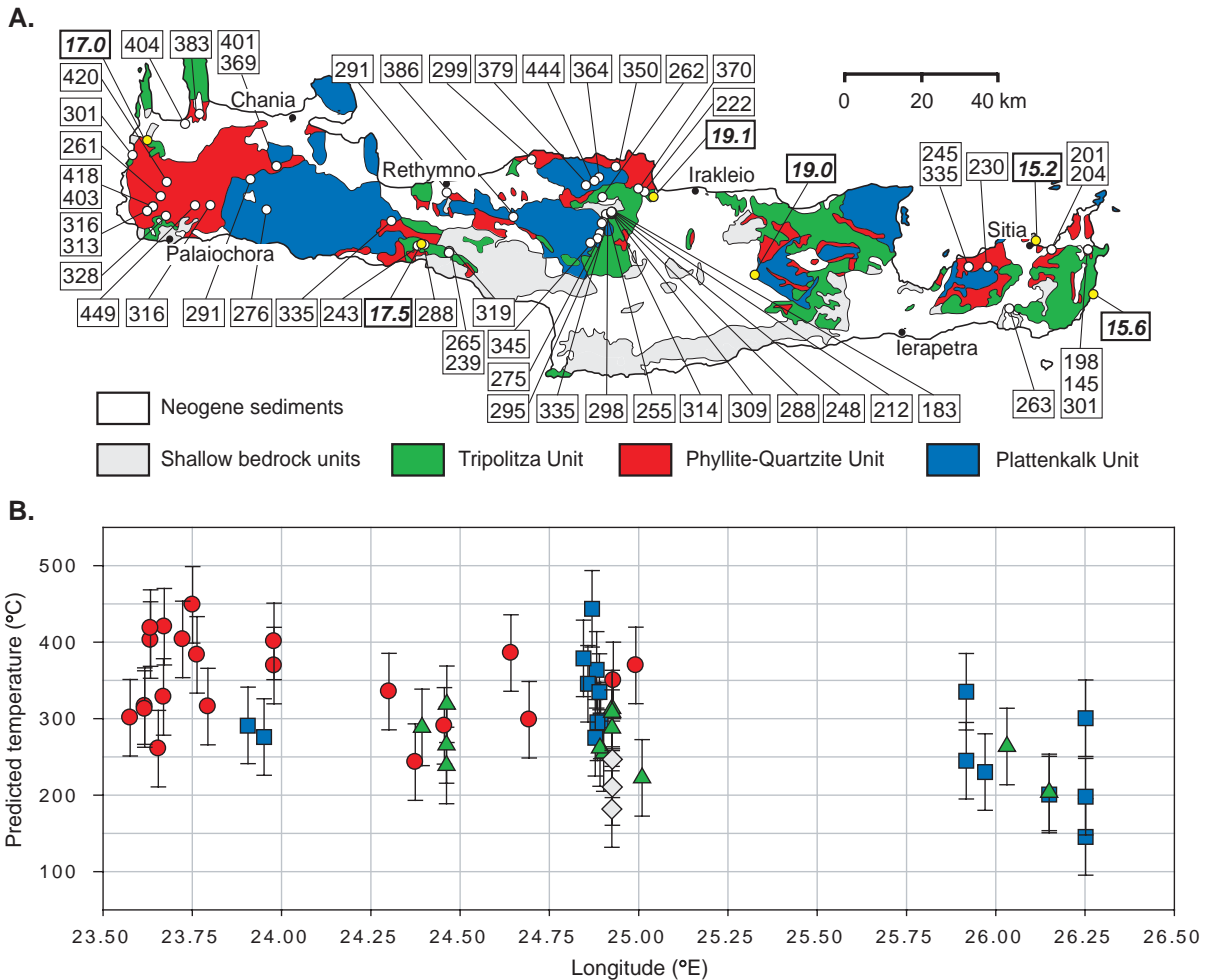


Fig. 8. (A) Simplified geologic map of Crete, after [54,65]. White circles denote sampled localities for RSCM analysis, yellow circles and bold-italic numbers denote apatite FT ages from the Tripolitza unit. Temperatures are in °C and FT ages are in Ma. The 17.5 ± 2.5 Ma age (TH208 from [54]) comes from a tuff in the Upper Triassic Ravdouca formation at the base of the Tripolitza. The remaining ages are from Eocene turbidites (“Tripolitza flysch”) at the top of the Tripolitza (TH2: 19.0 ± 1.0 Ma, TH41: 15.6 ± 1.5 Ma, TH45: 15.2 ± 2.2 Ma, TH56: 19.1 ± 1.5 Ma, TH134: 17.0 ± 2.3 Ma; S.N. Thomson, writ. comm., 2005). Uncertainties are cited at ± 1 SE. (B) RSCM temperatures from Crete as a function of longitude. Blue squares, Plattenkalk unit; red circles: Phyllite–Quartzite unit; green triangles, Tripolitza unit; and gray diamonds, Pindos flysch. See Appendix A for the detailed Raman data table.

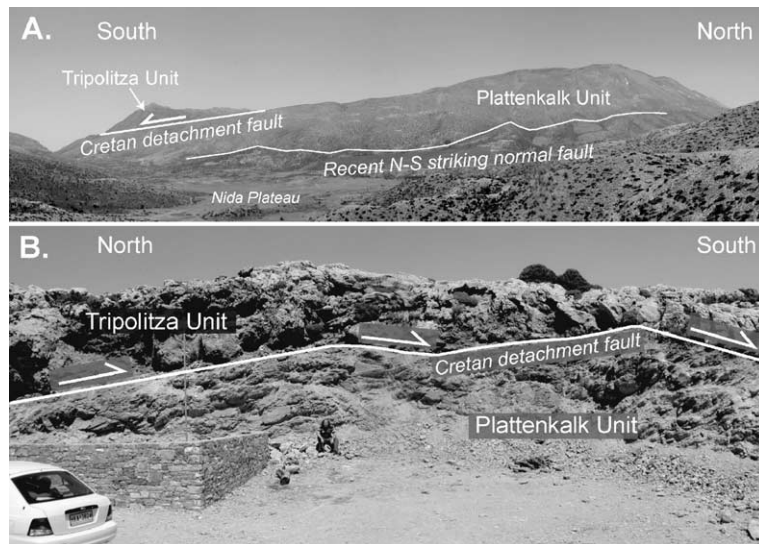


Fig. 9. (A) Photograph of the Cretan detachment fault in central Crete. (B) Close-up of the detachment fault showing the Tripolitza unit on top of the Plattenkalk unit.

do not contain evidence of Cenozoic metamorphism, suggesting a significant metamorphic break across the Cretan detachment.

The best evidence for HP–LT metamorphism comes from the PQ nappe, a package of Carboniferous to Triassic marine siliciclastic sediments, composed mainly of interbedded mudstones and quartzites. PQ mudstones in central and western Crete contain chloritoid \pm chlorite \pm pyrophyllite + muscovite + quartz + low albite + Fe- and Mg-carpholite [16]. This assemblage, along with the observation of coexisting pyrophyllite + low albite + lawsonite in rocks of the appropriate composition throughout the island, bracket maximum P – T conditions between 300 and 400 °C and 0.4 to 1.2 GPa [15,16,53]. Diagnostic metamorphic assemblages are generally lacking from the underlying PK nappe due to its mainly carbonate lithology, but an assemblage of Mg-carpholite + pyrophyllite + diasporite, locally present in a bauxite horizon in central Crete, indicates P – T conditions of \sim 0.7 GPa and 380 °C for the PK nappe [15]. Stratigraphic constraints and $^{40}\text{Ar}/^{39}\text{Ar}$ white mica ages indicate that peak metamorphic conditions occurred at 25 to 20 Ma [15,18]. FT zircon and apatite ages record slow cooling starting at \sim 20 Ma, followed by rapid cooling at \sim 10 Ma [19,48,53,54].

Thermochronometric data provide information about the exhumation history of higher units within the Cretan structural sequence. The Tripolitza nappe originated as a coherent sedimentary sequence with a maximum stratigraphic thickness of \sim 1200 m. It consists mainly of Triassic to middle Eocene carbonates,

capped by \sim 200 m of upper Eocene epiclastic turbidites [51]. Karakitsios ([55] as cited in [50]) reported a metamorphic temperature for the Tripolitza of 300 °C, estimated using the conodont color index. Metamorphic assemblages have not been recognized in the Tripolitza (which is not unexpected given its carbonate lithology), so estimates of metamorphic temperature and pressure are lacking. Thomson et al. [54] reported an FT apatite age of 17.5 Ma for a Triassic tuff from the base of the Tripolitza (Fig. 8). Thomson (writ. comm., 2005) dated five other FT apatite ages from the upper Eocene turbidites (locations and ages shown in Fig. 8). They give similar results as the tuff, indicating cooling of the unit below \sim 110 °C at 19 to 15 Ma. In contrast, the Uppermost unit preserves relatively old apatite FT ages, which indicate that this unit remained within the upper 4 to 7 km of the surface since 40 Ma [56].

We applied the modified RSCM thermometer to 53 samples from Crete (Fig. 8) to estimate the break in metamorphic temperature at the Cretan detachment. Our results for the PQ and PK nappes are consistent with published estimates from metamorphic equilibria, with metamorphic temperatures between 300 and 400 °C and a westward increase in temperature [15,16]. For instance, our data show that the average PK temperature is about 225 °C in easternmost Crete and increases to 340 °C in central Crete. Metamorphic temperatures in the PQ unit also increase from an average of 325 °C in central Crete to 365 °C in the western Crete. Our estimates are also consistent with the observed pattern of zircon FT resetting in the PQ unit [53]. In central and

western Crete, zircon FT ages for the PQ are younger than 20 Ma, and have been clearly reset during Cenozoic subduction and metamorphism. However, zircon FT ages from the PQ in eastern Crete are significantly older (>200 Ma), which indicates that metamorphism associated with Cenozoic subduction did not reach high enough temperatures to reset these ages. Our RSCM measurements for the PK nappe in eastern Crete indicate metamorphic temperatures of 225 °C. Although we have no measurements for the PQ nappe in eastern Crete, they likely were cooler than the estimate of 225 °C for the underlying PK nappe. Based on our experience with the zircon FT resetting in the Olympic Mountains, the unreset zircon FT ages in the PQ unit in eastern Crete probably indicate metamorphic temperatures below 200 °C.

We also obtained RSCM measurements from 12 samples from the Tripolitza nappe in eastern and central Crete. They indicate metamorphic temperatures ranging from 190 to 320 °C with an average of 250 °C. The variation around the average is probably not significant given that it has a magnitude similar to the ± 50 °C uncertainty associated with the thermometer. The metamorphic temperatures are consistent with the 300 °C indicated by conodont color index (see above). Several samples obtained from the Eocene flysch in the Tripolitza nappe indicate metamorphic temperatures between 290 and 325 °C. These results are important because they demonstrate that temperatures reported here occurred after accretion, and are thus related to late Cenozoic metamorphism in the Cretan subduction wedge rather than an earlier thermal event. Three measurements from Eocene flysch in the overlying Pindos unit give an average metamorphic temperature of 215 °C, confirming the overall upward decrease in metamorphic temperatures within the Cretan nappe sequence.

Most previous studies considered the Tripolitza to be “unmetamorphosed” [15,17–19,54,56,57]. In this context, the Cretan detachment has been viewed as the main structure responsible for tectonically exhuming the underlying HP–LT metamorphic rocks of Crete, as represented by the PK and PQ nappes. In central Crete (between longitude 24 and 25 °E), we have 7–10 samples each of the PK, PQ, and Tripolitza units; they indicate average metamorphic temperatures for these units of 345 °C, 325 °C, and 275 °C, respectively. The decrease in temperature is consistent with the decreasing structural position of these units. These data also indicate that the break in metamorphic temperature at the Cretan detachment is rather small, only about 50 to 70 °C.

If the Cretan detachment was responsible for exhumation of the PK and PQ units, thermochronometric constraints require that slip must have been fast [19,54]. The exhumation rate of ~ 4 km/m.y. estimated by Thomson et al. [19] implies a slip rate of 8 to 12 km/m.y. for a single fault with 20–30° dip. Based on regional correlations, Ring and Reischmann [58] estimated even higher slip rates, 20–30 km/m.y., for the Cretan detachment. Slip at these rates will cause rapid heating of the hangingwall block as it is juxtaposed against the relatively hot footwall, an effect that has been recognized at other fast-slip normal faults [59,60]. Thermal modeling by Ketcham [61] predicts an increase of hangingwall temperatures by 40–80 °C for normal faults with a slip rate above 10 km/m.y., and subsequent hangingwall cooling does not begin until slip on the normal fault decelerates or stops. In the case of Crete, exhumation is constrained to the interval 19 to 9 Ma. However, apatite FT ages from all parts of the Tripolitza (see above) show that at the beginning of this time interval, the hangingwall of the Cretan detachment was cooling rather than heating. This evidence precludes rapid slip on the Cretan detachment.

The absence of significant hangingwall heating indicates that our observations from the Tripolitza represent metamorphic temperatures prior to faulting. Thus, we can use the observed temperature break to estimate the thickness of the crustal section excised by the Cretan detachment. Maximum metamorphic conditions for the PQ unit in central Crete were about 350 °C and 0.9 GPa [16]. The pressure indicates a depth during metamorphism of ~ 34 km (assuming a crustal density of 2700 kg m⁻³). This corresponds to a pre-exhumation thermal gradient of ~ 10 °C/km (assuming a typical surface temperature of ~ 10 °C). Using this gradient, the 50 to 70 °C break, suggests that the Cretan detachment is responsible for only 5 to 7 km of the exhumation of the PQ and PK nappes.

This estimate is strongly dependent on the assumption that the thermal gradient is approximately linear. In subduction wedges, thermal gradients can be strongly nonlinear, but this situation tends to occur under the following conditions: 1) during the initial formation of a subduction zone, 2) when accretion, erosion or tectonic exhumation are fast (vertical velocities >0.5 km/m.y.), or 3) when internal radiogenic heat production is large (see [62] for details). Peak metamorphism of the PK and PQ units occurred at ~ 25 Ma, long after the Hellenic subduction wedge was initiated [49] and well before the start of rapid exhumation at 19 Ma. Thus, the thermal structure in the wedge should have had sufficient time to evolve to a steady-state thermal profile.

We infer that internal heat production was low within the wedge given that it was dominated by carbonates and quartzites. These arguments and observations indicate that thermal gradient in the subduction wedge was probably approximately linear at the time of peak metamorphism for the PQ and PK units.

The Cretan detachment remains an impressive structure that drops the Tripolitza down on to the PQ and PK units (Fig. 9). We agree with other workers that the structure is a major low-angle normal fault, an interpretation supported by abundant structural data [17–19]. However, the new temperature data presented here lead us to propose that the amount of exhumation accommodated by the detachment is only 5 to 7 km, significantly less than the >20 km postulated in previous papers. We are still left to explain the exhumation of the HP–LT metamorphic rocks of Crete from an initial depth of ~34 km. Erosion does not seem to be an important factor given that Crete did not emerge above sea level until ~12 Ma [49] and even then fission-track results from the Uppermost unit show that exhumation rates in the higher parts of the Cretan section were slow, ~200 m/m.y. [56]. Crete is cut by numerous high-angle normal faults that affect all of the basement units, including both the hangingwall and footwall of the detachment (e.g., [17,63,64]). Thus, we propose that the bulk of the remaining exhumation was accomplished by pervasive brittle thinning, rather than by fast slip on one or two isolated detachment faults.

6. Conclusions

The modified RSCM thermometer is a promising method that can be readily applied to obtain estimates of metamorphic temperature. Beyssac et al. [1] established that the thermometer is relatively insensitive to

pressures and thermal resetting and does provide reliable estimates of peak metamorphic temperatures. Our work here confirms the reliability of the thermometer and extends the applicable range to samples with metamorphic temperatures as low as 100 °C. The new calibration gives reasonable results for the low-grade metamorphic rocks of the Otago region in the South Island, New Zealand.

Application to the high-pressure units in the Crete yields results consistent with previously published metamorphic estimates. Furthermore, our measurements indicate a relatively small break in metamorphic temperature (<80 °C) at the Cretan detachment. This result indicates that the Cretan detachment played only a minor role in exhuming the young high-pressure metamorphic rocks of Crete.

Acknowledgements

Shun-Ichiro Karato, Zhenting Jiang, Phil Skemer, and Elizabeth Wong kindly provided assistance with the Raman spectroscopy equipment at Yale University. We thank Jay Ague, Eric Essene, Douwe van Hinsbergen, Stuart Thomson, and Elizabeth Wong for discussions; Karl Wegmann for help with sample collection; Olivier Beyssac and Gerd Rantitsch for critical reviews; and Ken Farley for editorial handling. In particular, we are grateful for comments by Gerd Rantitsch and Douwe van Hinsbergen that prompted us to consider the possibility of hangingwall heating above the Cretan detachment. Stuart Thomson kindly provided unpublished fission-track ages from Crete that proved essential for resolving this issue. This work was supported by NSF grants EAR-9814807 to Brandon and Ague, EAR-0208371 to Brandon, a grant from the Niarchos Foundation to Anderson, and an NSF Graduate Research Fellowship to Rahl.

Appendix A. New Raman measurements of carbonaceous material

Sample number	Unit	G position		G FWHM		D1 position		D1 FWHM		D1/G area		D1/G width		R1		R2		Predicted temperature (°C)	Latitude (°N)	Longitude (°E)
		Mean	SE	Mean	SE	Mean	SE	Mean	SE	Mean	SE	Mean	SE	Mean	SE	Mean	SE			
<i>Olympic Mountains, Washington State</i>																				
9	–	1596.50	8.56	38.54	6.06	1339.73	1.36	66.69	11.44	2.58	0.60	1.78	0.43	1.37	0.32	0.70	0.08	274	47.779	236.422
14	–	1604.35	3.97	37.35	5.53	1335.69	9.11	97.17	23.30	3.61	2.21	2.59	0.32	1.25	0.63	0.76	0.07	205	47.795	236.302
17	–	1599.96	2.02	37.90	5.32	1337.26	2.30	66.08	9.90	2.63	0.55	1.77	0.35	1.34	0.14	0.71	0.06	261	47.789	236.365
22	–	1601.85	0.45	35.40	1.38	1335.17	1.57	93.33	11.61	2.79	0.46	2.64	0.31	0.98	0.13	0.73	0.04	193	47.556	236.333
33	–	1607.25	1.14	34.15	0.65	1334.59	1.95	146.83	8.56	2.41	0.20	4.30	0.22	0.59	0.02	0.71	0.02	146	47.877	236.855
40	–	1606.36	1.07	37.09	1.52	1338.06	3.27	175.53	12.80	2.33	0.28	4.74	0.35	0.54	0.05	0.70	0.03	143	47.813	236.019
48	–	1595.18	9.79	43.59	11.00	1336.25	7.04	76.69	27.32	2.42	0.86	1.80	0.50	1.30	0.45	0.68	0.10	295	47.794	236.639
49	–	1599.89	1.63	42.34	4.86	1338.40	3.73	89.89	25.83	2.88	1.06	2.15	0.67	1.24	0.12	0.73	0.06	237	47.791	236.709
106	–	1595.87	7.19	66.61	14.48	1351.03	17.57	210.82	38.65	2.90	1.04	3.26	0.68	0.91	0.26	0.71	0.07	201	48.079	235.700
107	–	1603.05	2.85	46.22	6.78	1346.95	10.87	190.18	18.06	3.11	0.53	4.16	0.50	0.79	0.15	0.74	0.03	147	47.980	235.609
42b	–	1597.06	4.94	61.06	12.83	1361.21	14.11	223.78	70.91	3.37	0.82	3.66	0.95	0.99	0.31	0.76	0.04	166	47.640	236.615
<i>Otago Region, New Zealand</i>																				
000229-1	–	1576.24	2.56	29.26	20.04	1345.19	2.88	50.36	46.86	0.76	0.30	1.62	0.22	0.49	0.14	0.38	0.09	471	–45.589	170.103
000301-1b	–	1600.14	5.28	34.37	10.48	1331.93	2.62	89.53	25.99	2.78	0.30	2.62	0.29	0.98	0.15	0.73	0.03	193	–45.990	169.487
000303-1	–	1596.39	10.83	34.36	3.80	1333.62	6.68	113.66	32.15	2.87	0.68	3.26	0.65	0.86	0.20	0.72	0.07	186	–44.229	169.781
000303-4	–	1604.19	2.59	31.64	2.17	1332.06	2.28	111.78	12.97	3.03	0.36	3.53	0.26	0.81	0.08	0.75	0.02	145	–44.229	169.781
000304-2 XZ	–	1600.90	6.96	38.33	10.93	1331.92	2.72	126.75	32.87	3.18	0.68	3.33	0.29	0.93	0.23	0.75	0.04	161	–44.086	169.815
000304-5	–	1601.63	5.72	43.71	9.86	1338.99	3.95	111.45	38.17	3.08	0.47	2.53	0.49	1.22	0.25	0.74	0.04	224	–44.692	170.758
000305-7	–	1593.93	10.90	37.85	8.15	1333.79	6.16	120.42	27.77	3.07	0.69	3.26	0.82	0.94	0.18	0.73	0.08	191	–44.287	170.090
000305-8	–	1581.22	6.25	44.00	7.82	1342.79	2.99	64.79	16.31	2.60	0.63	1.47	0.28	1.70	0.37	0.67	0.04	331	–44.945	170.570
000307-4	–	1591.86	4.42	74.11	12.70	1353.00	18.34	253.83	59.54	3.84	1.23	3.44	0.67	1.13	0.25	0.78	0.06	165	–44.562	170.193
000311-2	–	1581.23	0.93	34.68	7.64	1352.64	0.86	95.97	29.96	1.32	0.34	2.39	0.34	0.52	0.08	0.48	0.05	369	–45.050	169.210
000311-3	–	1581.24	0.61	29.43	4.97	1353.86	1.38	84.62	31.69	1.09	0.27	2.38	0.49	0.49	0.05	0.45	0.04	393	–45.050	169.210
000311-4	–	1580.84	1.09	32.55	6.04	1350.35	1.29	85.50	29.45	1.05	0.31	2.29	0.36	0.46	0.08	0.43	0.05	412	–45.050	169.210
000312-1	–	1576.94	1.59	24.52	2.40	1345.65	1.76	33.42	3.71	0.88	0.25	1.37	0.13	0.68	0.18	0.44	0.07	450	–44.441	169.196
010313-3	–	1576.75	1.72	27.27	2.60	1345.63	1.39	38.39	5.13	0.97	0.26	1.41	0.17	0.72	0.22	0.45	0.07	441	–45.054	168.619
<i>Eastern Crete (east of 25 °E)</i>																				
040710-2-1	TR	1590.71	13.82	60.87	17.03	1354.56	6.49	192.96	12.23	3.54	0.87	3.44	1.09	1.10	0.22	0.74	0.06	203	35.196	26.150
040710-1-1	TR	1589.77	7.48	63.24	6.96	1343.94	3.93	153.83	21.94	4.00	0.91	2.46	0.41	1.57	0.26	0.73	0.05	263	35.050	26.031
040710-3-1	PK	1599.66	5.10	40.11	9.59	1331.90	3.30	144.59	24.09	3.31	0.26	3.67	0.52	0.90	0.11	0.77	0.01	145	35.196	26.252
040710-4A-1	PK	1600.10	6.16	46.13	10.66	1334.20	7.22	98.26	35.68	2.31	1.35	2.23	0.93	1.01	0.22	0.64	0.13	300	35.196	26.252
040710-4B-1	PK	1607.23	1.20	25.86	7.24	1282.44	23.08	105.79	18.77	2.10	0.62	4.21	0.61	0.61	0.17	0.66	0.05	198	35.196	26.252
040708-2-1	PK	1585.77	7.70	78.13	12.74	1365.49	14.51	249.32	68.60	3.43	0.81	3.16	0.81	1.15	0.30	0.75	0.04	200	35.196	26.150
040710-5-1	PK	1598.81	7.75	47.53	7.65	1340.35	2.92	127.96	23.29	3.55	0.94	2.70	0.34	1.26	0.25	0.73	0.05	230	35.154	25.970
040710-6A-1	PK	1603.86	2.74	42.81	8.07	1338.22	3.89	77.09	19.98	1.96	0.69	1.87	0.63	1.04	0.09	0.61	0.09	335	35.154	25.917
040710-6B-1	PK	1599.94	12.29	42.23	17.91	1339.92	7.98	100.50	35.43	2.91	0.92	2.45	0.37	1.14	0.23	0.70	0.08	245	35.154	25.917
062105-1	TRf	1578.99	31.70	66.42	27.78	1356.81	20.36	149.22	55.73	2.13	1.15	2.56	1.14	0.82	0.20	0.59	0.22	318	35.287	24.925
062105-2	TRf	1590.63	15.22	60.23	20.60	1336.53	16.88	166.93	83.60	1.98	1.33	2.97	1.67	0.66	0.17	0.56	0.24	312	35.288	24.925
062105-3	TRf	1584.39	20.72	68.30	27.30	1346.22	21.76	167.19	70.26	1.64	0.58	2.43	0.56	0.68	0.15	0.59	0.11	291	35.290	24.925
Tr4-1	TR	1592.53	5.31	55.54	14.48	1342.56	4.12	121.58	38.74	4.21	0.90	2.21	0.43	1.76	0.11	0.78	0.05	222	35.339	25.009
Tr5-1	TR	1576.65	11.27	82.41	14.32	1340.19	5.17	191.87	28.26	3.23	0.99	2.40	0.58	1.36	0.22	0.72	0.08	255	35.284	24.902

(continue on next page)

Appendix A (continued)

Sample number	Unit	G position		G FWHM		D1 position		D1 FWHM		D1/G area		D1/G width		R1		R2		Predicted temperature (°C)	Latitude (°N)	Longitude (°E)
		Mean	SE	Mean	SE	Mean	SE	Mean	SE	Mean	SE	Mean	SE	Mean	SE	Mean	SE			
<i>Central Crete (between longitude 24 and 25 °E)</i>																				
Tr2-1	TR	1597.46	4.69	53.93	12.64	1340.66	3.59	108.65	31.33	3.27	1.19	2.09	0.66	1.47	0.27	0.72	0.10	261	35.326	24.892
Tr7-1	TR	1595.72	11.13	62.99	20.88	1333.46	5.15	110.93	23.16	2.80	1.79	1.96	0.91	1.34	0.27	0.66	0.09	318	35.193	24.463
Tr8-1	TR	1600.42	3.77	45.82	6.16	1341.47	3.03	98.05	29.83	4.04	0.86	2.11	0.43	1.75	0.16	0.76	0.03	238	35.189	24.462
Tr9-1	TR	1594.06	9.34	56.98	24.15	1339.36	4.54	106.49	44.28	3.20	0.92	1.88	0.23	1.56	0.39	0.73	0.10	265	35.189	24.462
Tr10-1	TR	1596.22	5.12	48.02	8.70	1347.12	1.28	75.68	32.21	3.16	0.80	1.56	0.44	1.90	0.40	0.72	0.05	288	35.208	24.393
000601-1	PQ	1580.18	10.11	48.28	20.52	1344.86	9.95	88.43	54.62	2.04	1.11	1.73	0.58	1.16	0.34	0.59	0.13	369	35.347	24.992
010906-1	PQ	1577.54	5.82	35.72	10.27	1348.13	6.84	93.39	78.73	2.00	1.51	2.34	1.26	0.82	0.20	0.56	0.14	350	35.401	24.929
010904-1	PQ	1587.30	5.87	54.63	20.45	1345.57	8.83	131.96	76.53	2.92	1.59	2.21	0.76	1.25	0.42	0.67	0.15	298	35.419	24.693
010907-4	PQ	1580.64	4.34	35.33	7.33	1348.16	3.16	67.76	39.16	2.01	1.02	1.82	0.63	1.10	0.35	0.57	0.12	386	35.277	24.642
000703-2	PQ	1589.98	5.64	51.91	11.58	1344.48	6.01	134.32	65.45	2.75	1.31	2.44	0.93	1.09	0.24	0.66	0.12	290	35.337	24.456
010910-1B	PQ	1601.49	3.36	48.61	4.52	1345.97	2.03	89.43	18.44	2.90	0.49	1.83	0.26	1.44	0.11	0.74	0.03	243	35.205	24.375
010911-3	PQ	1581.38	5.16	46.22	12.32	1343.82	6.70	94.97	58.61	2.60	1.22	1.92	0.73	1.30	0.21	0.64	0.12	335	35.267	24.301
062105-5	PN	1591.89	7.47	57.54	15.56	1346.69	9.73	171.16	67.21	2.73	1.25	2.92	0.86	0.98	0.33	0.71	0.10	217	35.293	24.925
092105-6	PN	1600.64	6.43	66.48	16.95	1357.93	14.10	197.49	39.34	2.99	0.58	3.04	0.49	1.01	0.10	0.74	0.03	189	35.293	24.924
062105-4	PN	1595.55	14.61	43.47	17.67	1344.62	10.60	147.78	60.52	2.18	1.09	3.39	0.62	0.67	0.32	0.62	0.17	250	35.292	25.000
PK2-1	PK	1594.94	5.41	51.07	15.96	1343.79	7.05	75.08	39.31	2.91	0.89	1.47	0.57	1.96	0.32	0.71	0.07	297	35.265	24.893
PK3-1	PK	1592.38	12.90	58.07	16.01	1343.74	12.27	97.82	58.09	2.43	0.71	1.62	0.65	1.62	0.61	0.67	0.07	334	35.261	24.890
PK5-1	PK	1594.63	6.55	64.24	15.33	1346.94	18.82	144.46	91.60	2.62	0.99	2.11	1.08	1.47	0.76	0.69	0.09	295	35.236	24.885
PK11-1	PK	1590.74	2.17	43.69	7.00	1350.51	0.78	45.68	3.81	2.32	0.73	1.07	0.21	2.07	0.28	0.65	0.07	364	35.375	24.882
PK6-1	PK	1600.88	2.94	45.84	6.89	1347.56	1.37	70.15	27.52	3.05	0.72	1.51	0.38	1.86	0.34	0.73	0.06	275	35.224	24.878
PK10-1	PK	1583.62	5.60	36.07	11.67	1351.12	1.53	42.80	15.87	1.76	0.75	1.24	0.42	1.50	0.61	0.56	0.10	443	35.366	24.869
PK8-1	PK	1600.23	11.49	60.71	14.37	1347.02	11.42	103.70	51.51	2.14	1.33	1.70	0.76	1.19	0.24	0.62	0.12	345	35.213	24.858
K4	PK	1593.42	8.40	53.12	18.75	1348.57	6.57	65.76	34.73	2.06	0.67	1.24	0.34	1.54	0.22	0.62	0.09	378	35.355	24.845
<i>Western Crete (west of 24 °E)</i>																				
000631-1 AB	PQ	1585.51	5.20	39.99	12.02	1348.24	1.83	75.34	43.88	2.42	0.83	1.77	0.63	1.37	0.25	0.61	0.07	369	35.403	23.979
000631-1 XZ	PQ	1581.58	4.63	38.10	13.93	1346.62	3.26	64.53	50.43	1.91	0.79	1.58	0.59	1.22	0.26	0.57	0.09	401	35.403	23.979
000630-1	PQ	1589.68	6.19	58.90	16.13	1347.90	4.16	133.85	73.99	2.53	1.15	2.15	0.94	1.24	0.37	0.65	0.06	316	35.306	23.794
000623-1	PQ	1581.14	6.66	41.43	14.69	1347.22	2.56	96.70	57.13	2.40	2.33	2.34	1.02	0.89	0.45	0.54	0.12	383	35.531	23.763
000629-1	PQ	1581.53	5.57	34.26	9.90	1348.58	2.96	52.00	36.73	1.11	0.42	1.42	0.40	0.81	0.18	0.46	0.08	448	35.305	23.751
000623-3	PQ	1577.77	6.26	34.28	4.11	1346.59	3.96	55.64	9.73	1.08	0.39	1.62	0.20	0.66	0.16	0.48	0.07	403	35.507	23.723
000625-3	PQ	1586.62	6.00	45.59	11.42	1349.21	3.47	67.54	45.02	1.69	0.71	1.40	0.60	1.20	0.28	0.55	0.11	420	35.363	23.672
000627-1	PQ	1578.82	5.86	36.52	4.43	1345.64	4.14	73.15	36.23	2.10	0.49	1.96	0.86	1.13	0.22	0.63	0.04	328	35.279	23.669
000627-4	PQ	1589.12	5.46	52.14	12.36	1344.86	4.94	108.32	59.09	3.18	0.72	1.97	0.74	1.59	0.29	0.73	0.06	260	35.328	23.655
000626-3 AB	PQ	1582.32	5.28	32.42	4.01	1347.62	3.24	39.69	4.74	1.96	0.39	1.24	0.18	1.57	0.32	0.60	0.05	402	35.303	23.633
000626-3 XZ	PQ	1577.92	6.02	42.62	7.93	1342.70	4.11	62.44	28.87	1.85	0.77	1.44	0.47	1.26	0.36	0.56	0.08	418	35.303	23.633
000626-1	PQ	1578.61	4.42	42.63	4.72	1343.86	2.93	98.24	37.33	3.05	1.29	2.26	0.66	1.37	0.40	0.66	0.07	316	35.291	23.617
000626-2	PQ	1576.48	4.88	45.28	7.15	1342.80	4.51	108.12	32.76	3.00	0.98	2.38	0.59	1.26	0.35	0.66	0.07	312	35.291	23.617
000624-3	PQ	1593.51	4.41	65.11	12.54	1352.90	10.18	137.28	58.04	2.27	0.92	2.05	0.77	1.17	0.51	0.66	0.10	301	35.430	23.576
040708-8-1	PK	1596.29	14.05	43.59	26.03	1298.35	34.77	126.80	46.44	2.24	1.54	3.39	1.19	0.80	0.43	0.63	0.07	266	35.295	23.951
040708-4-1	PK	1587.02	4.65	46.72	9.61	1342.13	2.69	73.18	17.63	3.15	0.50	1.57	0.19	1.87	0.26	0.72	0.02	291	35.370	23.906

Note: Peaks in the Raman spectra were measured using the LabSpec peak fitting program. R1 and R2 reported here are averages of ten Raman spectra collected per sample. Uncertainties are represented by standard errors (SE), which were determined by dividing the standard deviation of the measurements by the square root of the number of measurements. PQ=Phyllite–Quartzite unit; PK=Plattenkalk unit; TR=Tripolitzta unit; TRf=flysch at the top of the Tripolitzta unit; PN=Pindos unit.

References

- [1] O. Beyssac, B. Goffé, C. Chopin, J.N. Rouzaud, Raman spectra of carbonaceous material in metasediments; a new geothermometer, *J. Metamorph. Geol.* 20 (2002) 859–871.
- [2] O. Beyssac, L. Bollinger, J.-P. Avouac, B. Goffé, Thermal metamorphism in the lesser Himalaya of Nepal determined from Raman spectroscopy of carbonaceous material, *Earth Planet. Sci. Lett.* 225 (2004) 233–241.
- [3] G. Rantitsch, W. Grogger, C. Teichert, F. Ebner, C. Hofer, E.-M. Maurer, B. Schaffer, M. Toth, Conversion of carbonaceous material to graphite within the Greywacke Zone of the Eastern Alps, *Int. J. Earth Sci.* 93 (2004) 959–973.
- [4] E.S. Grew, Carbonaceous material in some metamorphic rocks of New England and other areas, *J. Geol.* 82 (1974) 50–73.
- [5] J.D. Pasteris, B. Wopenka, Raman spectra of graphite as indicators of degree of metamorphism, *Can. Mineral.* 29 (1991) 1–9.
- [6] B. Wopenka, J.D. Pasteris, Structural characterization of kero-gens to granulite-facies graphite; applicability of Raman microprobe spectroscopy, *Am. Mineral.* 78 (1993) 533–557.
- [7] T.-F. Yui, E. Huang, J. Xu, Raman spectrum of carbonaceous material: a possible metamorphic grade indicator for low-grade metamorphic rocks, *J. Metamorph. Geol.* 14 (1996) 115–124.
- [8] F. Tuinstra, J.L. Koenig, Raman spectrum of graphite, *J. Chem. Phys.* 53 (1970) 1126–1130.
- [9] C. Bény-Bassez, J.N. Rouzaud, Characterization of carbonaceous materials by correlated electron and optical microscopy and Raman microspectroscopy, *Scanning Electron Microsc.* 1985 (1985) 119–132.
- [10] O. Beyssac, B. Goffé, J.P. Petit, E. Froigneux, M. Moreau, J.N. Rouzaud, On the characterization of disordered and heterogeneous carbonaceous materials using Raman spectroscopy, *Spectrochim. Acta, A* 59 (2003) 2267–2276.
- [11] M.H. Dodson, Kinetic processes and thermal history of slowly cooling solids, *Nature* 259 (1976) 551–553.
- [12] E.F. Baxter, Natural constraints on metamorphic reaction rates, in: D. Vance, W. Mueller, M. Villa Igor (Eds.), *Geochronology; linking the Isotopic Record with Petrology and textures*, Geological Society Special Publications, vol. 220, Geological Society of London, 2003, pp. 183–202.
- [13] O. Beyssac, F. Brunet, J.P. Petit, B. Goffé, J.N. Rouzaud, Experimental study of the microtextural and structural transformations of carbonaceous materials under pressure and temperature, *Eur. J. Mineral.* 15 (2003) 937–951.
- [14] M.T. Brandon, M.K. Roden-Tice, J.I. Garver, Late Cenozoic exhumation of the Cascadia accretionary wedge in the Olympic Mountains, Northwest Washington State, *Geol. Soc. Amer. Bull.* 110 (1998) 985–1009.
- [15] E. Seidel, H. Kreuzer, W. Harre, A late Oligocene/Early Miocene high pressure belt in the External Hellenides, *Geol. Jb.* 23 (1982) 165–206.
- [16] T. Theye, E. Seidel, O. Vidal, Carpholite, sudoite, and chloritoid in low-grade high-pressure metapelites from Crete and the Peloponnese, Greece, *Eur. J. Mineral.* 4 (1992) 487–507.
- [17] C. Fassoulas, A. Kiliyas, D. Mountrakis, Postnappe stacking extension and exhumation of high-pressure/low-temperature rocks in the Island of Crete, Greece, *Tectonics* 13 (1994) 125–138.
- [18] L. Jolivet, B. Goffé, P. Monié, C. Truffert-Luxey, M. Patriat, M. Bonneau, Miocene detachment in Crete and exhumation P-T-t paths of high pressure metamorphic rocks, *Tectonics* 15 (1996) 1129–1153.
- [19] S.N. Thomson, B. Stöckhert, M.R. Brix, Thermochronology of the high-pressure metamorphic rocks of Crete, Greece; implications for the speed of tectonic processes, *Geology (Boulder)* 26 (1998) 259–262.
- [20] G. Katagiri, I. Hideyuki, A. Ishitani, Raman spectra of graphite edge planes, *Carbon* 26 (1988) 565–571.
- [21] J.D. Pasteris, In situ analysis in geological thin-sections by Laser Raman microprobe microspectroscopy: a cautionary note, *Appl. Spectrosc.* 43 (1989) 567–570.
- [22] F.J. Pazzaglia, M.T. Brandon, A fluvial record of long-term steady-state uplift and erosion across the Cascadia forearc high, western Washington State, *Am. J. Sci.* 301 (2001) 385–431.
- [23] G.E. Batt, M.T. Brandon, K.A. Farley, M. Roden-Tice, Tectonic synthesis of the Olympic Mountains segment of the Cascadia wedge, using two-dimensional thermal and kinematic modeling of thermochronological ages, *J. Geophys. Res.* 106 (2001) 26731–26746.
- [24] M.T. Brandon, J.A. Vance, Tectonic evolution of the Cenozoic Olympic subduction complex, Washington State, as deduced from fission track ages for detrital zircons, *Am. J. Sci.* 292 (1992) 565–636.
- [25] R.J. Stewart, M.T. Brandon, Detrital-zircon fission-track ages for the “Hoh Formation”: implications for late Cenozoic evolution of the Cascadia subduction wedge, *Geol. Soc. Amer. Bull.* 116 (2004) 60–75.
- [26] M. Kasuya, C.W. Naeser, The effect of alpha-damage on fission-track annealing in zircon, *Nucl. Tracks Radiat. Meas.* 14 (1988) 477–480.
- [27] W.D. Carlson, R.A. Donelick, R.A. Ketcham, Variability of apatite fission-track annealing kinetics: I. Experimental results, *Am. Mineral.* 84 (1999) 1213–1223.
- [28] R.A. Ketcham, R.A. Donelick, W.D. Carlson, Variability of apatite fission-track annealing kinetics: III. Extrapolation to geological time scales, *Am. Mineral.* 84 (1999) 1235–1255.
- [29] R.A. Ketcham, R.A. Donelick, M.B. Donelick, AFTSolve: a program for multi-kinetic modeling of apatite fission-track data, *Geolog. Mater. Res.* 2 (2000) 1–32.
- [30] M.K. Rahn, M.T. Brandon, G.E. Batt, J.I. Garver, A zero-damage model for fission-track annealing in zircon, *Am. Mineral.* 89 (2004) 473–484.
- [31] C. Osborne, Statistical calibration: a review, *Int. Stat. Rev.* 59 (1991) 309–336.
- [32] R.J. Carroll, D. Ruppert, L.A. Stefanski, *Measurement Error in Nonlinear Models*, Chapman and Hall/CRC, 1995, 312 pp.
- [33] R.J. Carroll, D. Ruppert, The use and misuse of orthogonal regression in linear errors-in-variables models, *Am. Stat.* 50 (1996) 1–6.
- [34] C.-L. Cheng, J.W. van Ness, *Statistical Regression With Measurement Error*, Oxford University Press, 1999, 788 pp.
- [35] S.-C. Chow, J. Shao, On the difference between the classical and inverse methods of calibration, *Appl. Stat.* 39 (1990) 219–228.
- [36] W.A. Fuller, *Measurement Error Models*, Wiley, New York, 1987, 464 pp.
- [37] R.G. Krutchkoff, Classical and inverse regression methods of calibration, *Techonometrics* 9 (1967) 425–439.
- [38] P.R. Bevington, *Data Reduction and Error Analysis for the Physical Sciences*, McGraw-Hill Book Company, New York, NY, 1969, 336 pp.
- [39] B. Efron, R.J. Tibshirani, *An Introduction to the Bootstrap*, Chapman and Hall/CRC, 1994, 456 pp.

- [40] J. Carpenter, J. Bithell, Bootstrap confidence intervals: when, which, what? A practical guide for medical statisticians, *Stat. Med.* 19 (2000) 1141–1164.
- [41] N. Mortimer, A provisional structural thickness map of the Otago Schist, New Zealand, *Am. J. Sci.* 303 (2003) 603–621.
- [42] D.R. Gray, D.A. Foster, $^{40}\text{Ar}/^{39}\text{Ar}$ thermochronologic constraints on deformation, metamorphism and cooling/exhumation of a Mesozoic accretionary wedge, Otago Schist, New Zealand, *Tectonophysics* 385 (2004) 181–210.
- [43] D.S. Coombs, C.A. Landis, R.J. Norris, J.M. Sinton, D.J. Borns, D. Craw, The Dun Mountain Ophiolite Belt, New Zealand, its tectonic setting constitution and origin, with special reference to the southern portion, *Am. J. Sci.* 276 (1976) 561–603.
- [44] N. Mortimer, Jurassic tectonic history of the Otago Schist, New Zealand, *Tectonics* 12 (1993) 237–244.
- [45] N. Mortimer, Metamorphic discontinuities in orogenic belts: example of the garnet–biotite–albite zone in the Otago Schist, New Zealand, *International, J. Earth Sci.* 89 (2000) 295–306.
- [46] P.J.J. Kamp, Late Cretaceous–Cenozoic tectonic development of the southwest Pacific region, *Tectonophysics* 121 (1986) 225–251.
- [47] Y. Nishimura, D.S. Coombs, C.A. Landis, T. Itaya, Continuous metamorphic gradient documented by graphitization and K–Ar age, southeast Otago, New Zealand, *Am. Mineral.* 85 (2000) 1625–1636.
- [48] J.M. Rahl, Tectonic evolution of the Hellenic (Greece) and Otago (New Zealand) subduction wedges, Ph.D. thesis, Yale University, 2005, 208 pp.
- [49] J.E. Meulenkamp, M.J.R. Wortel, W.W.A. van, W. Spakman, S.E. Hoogerduyn, On the Hellenic subduction zone and the geodynamic evolution of Crete since the late middle Miocene, *Tectonophysics* 146 (1988) 203–215.
- [50] M. Bonneau, Correlation of the Hellenic Nappes in the south-east Aegean and their tectonic reconstruction, in: J.E. Dixon, A.H.F. Robertson (Eds.), *The geological evolution of the eastern Mediterranean*, Geological Society Special Publications 17, Geological Society of London, London, United Kingdom, 1984, pp. 517–527.
- [51] R. Hall, M.G. Audley-Charles, D.J. Carter, The significance of Crete for the evolution of the eastern Mediterranean, in: J.E. Dixon, A.H.F. Robertson (Eds.), *The geological evolution of the eastern Mediterranean*, Geological Society Special Publications 17, Geological Society of London, London, United Kingdom, 1984, pp. 499–517.
- [52] G.S. Lister, G. Banga, A. Feenstra, Metamorphic core complexes of Cordilleran type in the Cyclades, Aegean Sea, Greece, *Geology (Boulder)* 12 (1984) 221–225.
- [53] M.R. Brix, B. Stöckhert, E. Seidel, T. Theye, S.N. Thomson, M. Küster, Thermobarometric data from a fossil zircon partial annealing zone in high pressure–low temperature rocks of eastern and central Crete, Greece, *Tectonophysics* 349 (2002) 309–326.
- [54] S.N. Thomson, B. Stöckhert, M.R. Brix, Miocene high-pressure metamorphic rocks of Crete, Greece; rapid exhumation by buoyant escape, in: U. Ring, T. Brandon Mark, S. Lister Gordon, D. Willett Sean (Eds.), *Exhumation Processes: Normal Faulting, Ductile Flow and Erosion*, Geological Society Special Publications, vol. 154, Geological Society of London, London, United Kingdom, 1999, pp. 87–107.
- [55] V. Karakitsios, Contribution à l'Étude Géologique des Hellénides: Etude de la Région de Sellia (Crète moyenne-occidentale, Grèce), Thèse Doctorat 3e cycle, University P. et M. Curie, 1979, 167 pp.
- [56] S.N. Thomson, B. Stöckhert, H. Rauche, M.R. Brix, Apatite fission-track thermochronology of the Uppermost Tectonic Unit of Crete, Greece: implications for the post-Eocene evolution of the Hellenic subduction system, in: P. Van Den Haute, F. De Corte (Eds.), *Advances in Fission-Track Thermochronology*, Kluwer Academic Publishers, 1998, pp. 187–205.
- [57] U. Ring, P.W. Layer, T. Reischmann, Miocene high-pressure metamorphism in the Cyclades and Crete, Aegean Sea, Greece; evidence for large-magnitude displacement on the Cretan detachment, *Geology (Boulder)* 29 (2001) 395–398.
- [58] U. Ring, T. Reischmann, The weak and superfast Cretan Detachment, Greece: exhumation at subduction rates in extruding wedges, *J. Geol. Soc. (Lond.)* 159 (2002) 225–228.
- [59] I. Dunkl, B. Grasemann, W. Frisch, Thermal effects of exhumation of a metamorphic core complex on hanging wall syn-rift sediments: an example from the Rechnitz Window, Eastern Alps, *Tectonophysics* 297 (1998) 31–50.
- [60] B. Grasemann, I. Dunkl, Effects of the geometry of normal faulting on the near surface heat flow during extension: the example of the Rechnitz Metamorphic Core Complex (Austria), *Mitt. Inst. Österr. Gesch.Forsch.* 93 (2003) 87–103.
- [61] R.A. Ketchum, Thermal models of core-complex evolution in Arizona and New Guinea; implications for ancient cooling paths and present-day heat flow, *Tectonics* 15 (1996) 933–951.
- [62] L.H. Royden, The steady state thermal structure of eroding orogenic belts and accretionary prisms, *J. Geophys. Res., B, Solid Earth Planets* 98 (1993) 4487–4507.
- [63] J. Angelier, N. Lyberis, P.X. Le, E. Barrier, P. Huchon, The tectonic development of the Hellenic Arc and the Sea of Crete; a synthesis, *Tectonophysics* 86 (1982) 159–196.
- [64] J.H. ten Veen, P.T. Meijer, Late Miocene to Recent tectonic evolution of Crete (Greece): geological observations and model analysis, *Tectonophysics* 298 (1998) 191–208.
- [65] N. Creutzburg, C.W. Drooger, J.E. Meulenkamp, Crete Island, *Inst. Geol. and Min. Res., Sect. Geol. Mapping, Greece*, 1977, 2 sheets pp.